PHYSICAL REVIEW E **100**, 042408 (2019)

Stimulated echo double diffusion encoded imaging of closed pores: Influence and removal of unbalanced terms

Kerstin Demberg,[1,2] Frederik Bernd Laun,[3] Peter Bachert,[1,2] Mark Edward Ladd,[1,2,4] and Tristan Anselm Kuder[1,*]
[1]*Medical Physics in Radiology, German Cancer Research Center (DKFZ), Heidelberg, Germany*
[2]*Faculty of Physics and Astronomy, Heidelberg University, Heidelberg, Germany*
[3]*Institute of Radiology, University Hospital Erlangen, Friedrich-Alexander-Universität Erlangen-Nürnberg (FAU), Erlangen, Germany*
[4]*Faculty of Medicine, Heidelberg University, Heidelberg, Germany*

(Received 4 April 2019; published 15 October 2019)

Nuclear magnetic resonance (NMR) diffusion pore imaging has been proposed to study the shape of arbitrary closed pores filled with an NMR-detectable medium by use of nonclassical diffusion encoding schemes. Potential applications can be found in biomedical imaging and porous media research. When studying non-point-symmetric pores, NMR signals with nonvanishing imaginary parts arise containing the pore shape information, which is lost for classical diffusion encoding schemes. Key limitations are the required high magnetic field gradient amplitudes and $T2$ relaxation while approaching the diffusion long-time limit. To benefit from the slower $T1$ decay, we demonstrate the feasibility of diffusion pore imaging with stimulated echoes using Monte Carlo simulations and experiments with hyperpolarized xenon-129 gas in well-defined geometries and show that the necessary complex-valued signals can be acquired. Analytical derivation of the stimulated echo double diffusion encoded signal was performed to investigate the effect of the additionally arising undesired terms on the complex phase information. These terms correspond to signals arising for spin-echo sequences with unbalanced gradients. For most possible applications, the unbalanced terms can be neglected. If non-negligible, selection of the appropriate signal component using a phase cycling scheme was demonstrated experimentally. Using stimulated echoes may be a step towards application of diffusion pore imaging to larger pores with gradient amplitudes available today in preclinical systems.

DOI: 10.1103/PhysRevE.100.042408

I. INTRODUCTION

Nuclear magnetic resonance (NMR) diffusion experiments are widely employed in medical imaging and porous media research to probe diffusion barriers via Brownian motion of NMR-detectable atoms or molecules enabling, for example, the detection of tumor lesions [1–8]. Mostly spin-echo sequences are used, which results in a considerable signal loss due to T_2 relaxation at longer echo and diffusion times limiting the size of the restrictions that can be probed.

This limitation can be resolved using stimulated echoes [9–19]. Stimulated echoes are generated by a $(90^\circ - t_1 - 90^\circ - t_2 - 90^\circ - t_3)$ sequence: The transverse magnetization generated by the first 90° radio frequency (rf) pulse is dephased by a first diffusion encoding gradient pulse during t_1 and is then stored longitudinally after the second rf pulse. During t_2 only the longitudinal component decaying with the relaxation time T_1 survives. A third rf pulse generates transverse magnetization that is partly rephased by a second diffusion gradient pulse during t_3 yielding a stimulated echo after t_3. By prolonging t_2, long diffusion times can be reached while maintaining sufficient signal, since the relevant T_1 relaxation is typically an order of magnitude slower compared to T_2 relaxation. The longer diffusion time can be used to study slow diffusion rates; to remove artifacts from, e.g., background gradients which have no effect during z storage [20]; to compensate unavailability of gradient power [10]; or to reach the diffusion long-time limit [21–23].

This work extends the utilization of stimulated echoes to nonconventional gradient profiles that preserve phase information about the structure of diffusion restrictions [24], and to diffusion pore imaging (DPI). DPI enables measurement of the average shape of arbitrary closed pores in the considered volume element [25] at a much increased signal-to-noise ratio (SNR) compared to conventional NMR microscopy [26–32]. For stimulated echo diffusion encoded experiments, only the magnitude of the diffusion encoded signal has been considered and measured so far [33–35]. Nonetheless, DPI relies on obtaining complex-valued diffusion encoded signals [25]. Generation of the complex diffusion encoded signals is realized either with long-narrow gradient profiles [25–29,31,36,37] or with double diffusion encoded (DDE) experiments [30,38,39]. In contrast to the long-narrow approach, the DDE approach is based solely on short gradient pulses and allows utilizing stimulated echoes to reach the long-time limit. This might be a step towards application of diffusion pore imaging to larger pores demanding lower gradient strengths, since the necessary high gradient amplitude is a major current limitation.

A general property of using diffusion encoded pulse sequences with stimulated echoes is the fact that not only the

---

[*] Corresponding author: German Cancer Research Center (DKFZ), Medical Physics in Radiology, Im Neuenheimer Feld 280, D-69120 Heidelberg; t.kuder@dkfz.de

signal corresponding to a spin-echo sequence with balanced gradients arises but additional unbalanced terms occur as previously described by Khrapitchev and Callaghan [14]. Here, we extend their approach to diffusion encoded signals with explicitly nonvanishing imaginary parts, investigate the effect of the additional terms on the final signal, and show that the full pore space function can be reconstructed from stimulated echo DDE experiments.

II. THEORY

A. Diffusion pore imaging

A pore with volume V filled with an NMR-detectable diffusing medium is defined by the pore space function $\rho(\boldsymbol{x})$ which equals V^{-1} inside the pore and 0 outside. Using pore imaging techniques, $\rho(\boldsymbol{x})$ is determined by measuring its Fourier transform $\tilde{\rho}(\boldsymbol{q}) = \int_{\text{Pore}} \rho(\boldsymbol{x}) e^{-i\boldsymbol{q}\boldsymbol{x}} d\boldsymbol{x}$, which is also referred to as the "form factor" with the q-space [40] vector $\boldsymbol{q}$. For non-point-symmetric pores, $\tilde{\rho}(\boldsymbol{q})$ is complex [24,36,39]. To measure the phase information $\psi(\boldsymbol{q}) = \arg[\tilde{\rho}(\boldsymbol{q})]$, double diffusion encoded (DDE) measurements [41] can be used, from which the phase of $\tilde{\rho}(\boldsymbol{q})$ can be extracted [30,38,39,42].

B. Double diffusion encoding and q-space imaging with stimulated echoes

This section roughly sketches the derivation of the DDE and q-space signals for stimulated echo sequences; details can be found in the Appendix. In this section, idealized rf pulses are assumed ignoring other possible coherent echo paths arising from experimentally imperfect rf pulses. As described in [14], an NMR pulse sequence imprints specific phase factors on diffusing spin packets. Using the rotating reference frame and treating transverse magnetization as complex numbers, a gradient pulse [amplitude $\boldsymbol{G}_i$, duration δ, start time t, gyromagnetic ratio γ; see Figs. 1(a) and 1(b)] imprints the factor $e^{i\varphi_i}$ on the spin packet with $\varphi_i = -\gamma \int_t^{t+\delta} \boldsymbol{G}_i\, \boldsymbol{x}(t')dt'$. Storing the magnetization in the longitudinal direction and assuming complete dephasing of transverse components, followed by a flip back to the transverse plane, e.g., using $90^\circ_{\alpha_1}$ and $90^\circ_{\alpha_2}$ in Fig. 1(a), is equivalent to taking the real part of the magnetization with appropriate phase factors according to the pulse phases α_j as defined in Fig. 1(c) so that $e^{i\varphi}$ is transformed to $-\frac{1}{2}(e^{i(\varphi-\alpha_1+\alpha_2)} + e^{-i(\varphi-\alpha_1-\alpha_2)})$ [14]. Due to taking the real part, the application of stimulated echo diffusion encoding results in a superposition of terms originating from different magnetization pathways, which reflect contributions corresponding to both balanced and unbalanced gradients [14], so that the concept of fully balanced diffusion encoding gradients is not applicable to stimulated echoes. For a DDE sequence with stimulated echoes as depicted in Fig. 1(a), the phase factor for the case $\alpha_j = 0$ is given by

$$\frac{1}{4}\Big\{e^{i(\frac{\varphi_1}{2}-\varphi_2+\frac{\varphi_3}{2})} + e^{i(\frac{\varphi_1}{2}+\varphi_2+\frac{\varphi_3}{2}+2\vartheta)} + e^{i(-\frac{\varphi_1}{2}-\varphi_2+\frac{\varphi_3}{2}-\vartheta)} + e^{i(-\frac{\varphi_1}{2}+\varphi_2+\frac{\varphi_3}{2}+\vartheta)}\Big\}, \qquad (1)$$

where the first term equals the phase term arising for a balanced spin-echo sequence with antiparallel wave vectors. The three other terms correspond to spin-echo encodings with unbalanced gradients causing phases $\vartheta = -\gamma\delta\boldsymbol{G}_2\boldsymbol{x}_{\text{cm}} = \boldsymbol{q}\boldsymbol{x}_{\text{cm}}$ for spins located in a pore shifted by $\boldsymbol{x}_{\text{cm}}$ from the origin introducing a dependency on the center of mass position in Eq. (1) when considering pores. For arbitrary α_j different superpositions of the four terms in Eq. (1) are obtained.

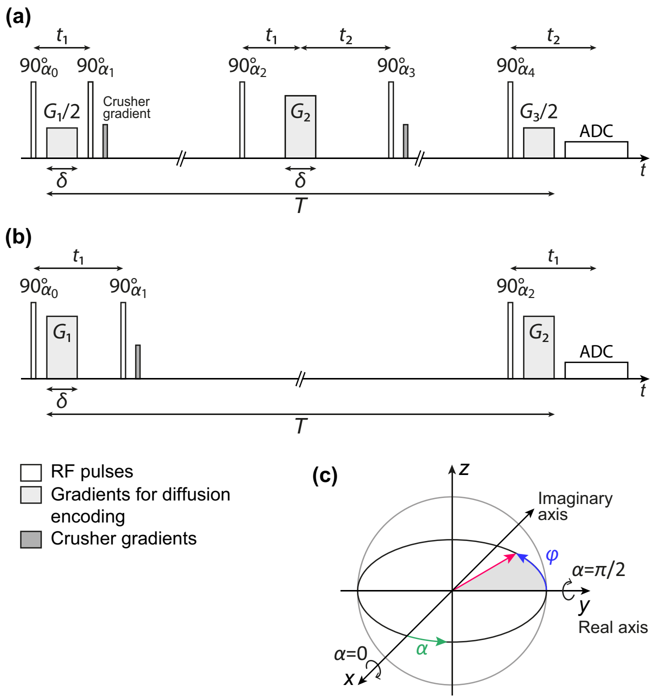

FIG. 1. Schemes of the stimulated echo sequences for (a) double diffusion encoding and (b) q-space imaging. α_j denotes the phase of the respective rf pulse. (c) The complex magnetization vector (red) with phase φ (blue) lies in the transverse plane of the right-handed rotating reference frame. With the convention that the excitation field B_1 points along the x axis for $\alpha = 0$ as in [14,44] and choosing the real axis along y, a 90° rf pulse with $\alpha = 0$ generates real magnetization and a pulse with $\alpha = \pi/2$ generates imaginary magnetization along the negative x axis.

Usually, the unbalanced terms can be neglected when describing the diffusion-encoded stimulated echo signal, since large sample or voxel sizes l with homogeneous pore distributions are assumed. In a simple approach, the pore distribution can be approximated with a box function, $P_{x_{\text{cm}}}(x_{\text{cm}}) = l^{-1}\text{rect}_l(x_{\text{cm}})$, whose Fourier transform is given by a sinc function, $P_{x_{\text{cm}}}(q) = \text{sinc}(ql/2)$, which decays to zero rapidly. For the wave vectors used to probe the pore sizes, the magnitude of $P_{x_{\text{cm}}}(q)$ converges to zero, as these are much larger than those used to probe structures on the voxel size scale, which yields a fast decay of the unbalanced terms compared to the balanced ones. In the further evaluation, the unbalanced terms are included nonetheless and the pores' center of mass distribution $P_{\boldsymbol{x}_{\text{cm}}}(\boldsymbol{x})$ is introduced to analyze the effect of these terms on the measured DDE phase and to check whether the induced changes are relevant for DDE phase-based diffusion pore imaging.

TABLE I. Phase cycling scheme for double diffusion encoding.

	Rf pulses					Balanced term	Unbalanced terms		
S_3	1	2	3	4	5	$A = e^{i(\frac{\varphi_1}{2}-\varphi_2+\frac{\varphi_3}{2})}$	$B = e^{i(\frac{\varphi_1}{2}+\varphi_2+\frac{\varphi_3}{2})}$	$C = e^{i(-\frac{\varphi_1}{2}-\varphi_2+\frac{\varphi_3}{2})}$	$D = e^{i(-\frac{\varphi_1}{2}+\varphi_2+\frac{\varphi_3}{2})}$
I	α_0	α_1	α_2	α_3	α_4	+[a]	+	+	+
II	α_0	$\alpha_1 + \frac{\pi}{2}$	$\alpha_2 + \frac{\pi}{2}$	$\alpha_3 + \frac{\pi}{2}$	$\alpha_4 + \frac{\pi}{2}$	+	+	−	−
III	α_0	α_1	α_2	$\alpha_3 + \frac{\pi}{2}$	$\alpha_4 + \frac{\pi}{2}$	−	+	−	+
IV	α_0	$\alpha_1 + \frac{\pi}{2}$	$\alpha_2 + \frac{\pi}{2}$	α_3	α_4	−	+	+	−
			+I + II − III − IV →			4[a]	0	0	0

[a] Only the sign is tabulated. Depending on the values of $\alpha_0 - \alpha_4$ phase factors arise according to Eq. (2), but they are identical within each column.

Integrating over all random walk trajectories (for details see the Appendix) yields for arbitrary α_j the signal

$$S_{3,\mathrm{STE}}(\boldsymbol{q}) = \tfrac{1}{4}\{e^{i(\alpha_0-\alpha_1-\alpha_2+\alpha_3+\alpha_4)}\tilde{\rho}^*(\boldsymbol{q}/2)^2\tilde{\rho}(\boldsymbol{q}) + e^{i(\alpha_0-\alpha_1+\alpha_2-\alpha_3+\alpha_4)}\tilde{P}^*_{\boldsymbol{x}_{\mathrm{cm}}}(2\boldsymbol{q})\tilde{\rho}^*(\boldsymbol{q}/2)^2\tilde{\rho}^*(\boldsymbol{q})$$
$$+ e^{i(-\alpha_0+\alpha_1-\alpha_2+\alpha_3+\alpha_4)}\tilde{P}_{\boldsymbol{x}_{\mathrm{cm}}}(\boldsymbol{q})|\tilde{\rho}(\boldsymbol{q}/2)|^2\tilde{\rho}(\boldsymbol{q}) + e^{i(-\alpha_0+\alpha_1+\alpha_2-\alpha_3+\alpha_4)}\tilde{P}^*_{\boldsymbol{x}_{\mathrm{cm}}}(\boldsymbol{q})|\tilde{\rho}(\boldsymbol{q}/2)|^2\tilde{\rho}^*(\boldsymbol{q})\}, \quad (2)$$

with the Fourier transform $\tilde{P}_{\boldsymbol{x}_{\mathrm{cm}}}(\boldsymbol{q})$ of $P_{\boldsymbol{x}_{\mathrm{cm}}}(\boldsymbol{x})$, and the asterisks indicate complex conjugates. The first, balanced term contains the desired DDE spin-echo signal,

$$S_{3,\mathrm{SE}}(\boldsymbol{q}) = \tilde{\rho}^*(\boldsymbol{q}/2)^2\tilde{\rho}(\boldsymbol{q}) \quad (3)$$

[38,39], from which the form factor phase can be derived. Proceeding analogously for the q-space imaging sequence in Fig. 1(b) results in

$$S_{2,\mathrm{STE}}(\boldsymbol{q}) = -\tfrac{1}{2}\{e^{i(-\alpha_0+\alpha_1+\alpha_2)}|\tilde{\rho}(\boldsymbol{q})|^2 + e^{i(\alpha_0-\alpha_1+\alpha_2)}\tilde{P}^*_{\boldsymbol{x}_{\mathrm{cm}}}(2\boldsymbol{q})\tilde{\rho}^*(\boldsymbol{q})^2\}, \quad (4)$$

with the spin-echo q-space imaging signal $S_{2,\mathrm{SE}}(\boldsymbol{q}) = |\tilde{\rho}(\boldsymbol{q})|^2$ comprised in the first term. The unbalanced terms, three of them for the DDE signal and one for the q-space signal, are thus sensitive to pore translations and modulated by $\tilde{P}_{\boldsymbol{x}_{\mathrm{cm}}}(\boldsymbol{q})$, contrary to the spin-echo approach.

C. Phase cycling

To eliminate the unbalanced terms containing $\tilde{P}_{\boldsymbol{x}_{\mathrm{cm}}}(\boldsymbol{q})$ in Eqs. (2) and (4), phase cycling can be used, as discussed in Ref. [14]. Tables I and II propose the necessary rf pulse phases for stimulated echo pore imaging. Acquiring the signals corresponding to rows I – IV and calculating +I + II − III − IV yields the $e^{i(\frac{\varphi_1}{2}-\varphi_2+\frac{\varphi_3}{2})}$ term resulting in the desired balanced term $\tilde{\rho}^*(\boldsymbol{q}/2)^2\tilde{\rho}(\boldsymbol{q})$. For arbitrary α_j, this approach is still valid, since only the relative phases between the table rows are relevant. In Table II, the phase cycle for q-space imaging is listed.

D. Distribution of different pore space functions

Pores of M different sizes or shapes with the pore space functions $\rho_n(\boldsymbol{x})$, volumes V_n, and center of mass distribution $P_{n,\boldsymbol{x}_{\mathrm{cm}}}(\boldsymbol{x})$ are considered yielding the total DDE signal attenuation,

$$S_{3,\mathrm{STE,tot}}(\boldsymbol{q}) = \sum_{n=1}^{M} f_n \frac{1}{4}\{e^{i(\alpha_0-\alpha_1-\alpha_2+\alpha_3+\alpha_4)}\tilde{\rho}^*_n(\boldsymbol{q}/2)^2\tilde{\rho}_n(\boldsymbol{q}) + e^{i(\alpha_0-\alpha_1+\alpha_2-\alpha_3+\alpha_4)}\tilde{P}^*_{n,\boldsymbol{x}_{\mathrm{cm}}}(2\boldsymbol{q})\tilde{\rho}^*_n(\boldsymbol{q}/2)^2\tilde{\rho}^*_n(\boldsymbol{q})$$
$$+ e^{i(-\alpha_0+\alpha_1-\alpha_2+\alpha_3+\alpha_4)}\tilde{P}_{n,\boldsymbol{x}_{\mathrm{cm}}}(\boldsymbol{q})|\tilde{\rho}_n(\boldsymbol{q}/2)|^2\tilde{\rho}_n(\boldsymbol{q}) + e^{i(-\alpha_0+\alpha_1+\alpha_2-\alpha_3+\alpha_4)}\tilde{P}^*_{n,\boldsymbol{x}_{\mathrm{cm}}}(\boldsymbol{q})|\tilde{\rho}_n(\boldsymbol{q}/2)|^2\tilde{\rho}^*_n(\boldsymbol{q})\}, \quad (5)$$

with $f_n = V_n/(\sum_{n=1}^{M} V_n)$. For q-space imaging, the total signal is

$$S_{2,\mathrm{STE,tot}}(\boldsymbol{q}) = -\sum_{n=1}^{M} f_n \frac{1}{2}\{e^{i(-\alpha_0+\alpha_1+\alpha_2)}|\tilde{\rho}_n(\boldsymbol{q})|^2 + e^{i(\alpha_0-\alpha_1+\alpha_2)}\tilde{P}^*_{n,\boldsymbol{x}_{\mathrm{cm}}}(2\boldsymbol{q})\tilde{\rho}^*_n(\boldsymbol{q})^2\}. \quad (6)$$

Total spin-echo signals are $S_{3,\mathrm{SE,tot}}(\boldsymbol{q}) = \sum_{n=1}^{M} f_n\tilde{\rho}^*_n(\boldsymbol{q}/2)^2\ \tilde{\rho}_n(\boldsymbol{q})$ and $S_{2,\mathrm{SE,tot}}(\boldsymbol{q}) = \sum_{n=1}^{M} f_n|\tilde{\rho}_n(\boldsymbol{q})|^2$ [43].

III. METHODS

A. Derivation of the form factor

To extract the form factor's phase $\psi(\boldsymbol{q}) = \arg[\tilde{\rho}(\boldsymbol{q})]$ from the DDE signal following Ref. [39], $\tilde{\rho}(\boldsymbol{q})$ and $S_{3,\mathrm{SE}}(\boldsymbol{q})$ are written in terms of magnitude and phase; i.e., $\tilde{\rho}(\boldsymbol{q}) = A(\boldsymbol{q})e^{i\psi(\boldsymbol{q})}$ and $S_{3,\mathrm{SE}}(\boldsymbol{q}) = B(\boldsymbol{q})e^{i\omega(\boldsymbol{q})}$, where $A(\boldsymbol{q}) = \sqrt{S_{2,\mathrm{SE}}(\boldsymbol{q})}$ is obtained from the q-space measurement. Inserting both into Eq. (3) results in

$$B(\boldsymbol{q})e^{i\omega(\boldsymbol{q})} = A(\boldsymbol{q}/2)^2e^{-2i\psi(\boldsymbol{q}/2)}A(\boldsymbol{q})e^{i\psi(\boldsymbol{q})}. \quad (7)$$

TABLE II. Phase cycling scheme for q-space imaging.

	Rf pulses			Balanced term	Unbalanced term
S_2	1	2	3	$A = e^{i(-\varphi_1+\varphi_2)}$	$B = e^{i(\varphi_1+\varphi_2)}$
I	α_0	α_1	α_2	–[a]	–
II	α_0	$\alpha_1 + \frac{\pi}{2}$	$\alpha_2 + \frac{\pi}{2}$	+	–
		−I + II →		2[a]	0

[a] Only the sign is tabulated. Depending on the values of α_0, α_1, α_2, phase factors arise according to Eq. (4), but they are identical within each column.

Since $A(\boldsymbol{q})$ and $B(\boldsymbol{q})$ are real and positive, the following recursive equation arises:

$$\psi(\boldsymbol{q}) = 2\psi(\boldsymbol{q}/2) + \omega(\boldsymbol{q}). \tag{8}$$

Now, radial acquisitions of $S_{3,\mathrm{SE}}(\boldsymbol{q})$ are considered; i.e., $\boldsymbol{q} = \boldsymbol{n}q$ with constant gradient direction $\boldsymbol{n}$ and increasing $q > 0$. Using the measurement $\omega(\boldsymbol{q}) = \arg[(S_{3,\mathrm{STE}}(\boldsymbol{q})]$ and the initial conditions $\psi(q_0 = 0) = 0$ and $\partial\psi(\boldsymbol{n}q)/\partial q|_{q=0} = 0$, Eq. (8) was recursively solved for the measured q values q_i by setting $\psi(\boldsymbol{n}q_1) = 0$ which allows obtaining $\psi(\boldsymbol{n}q_2)$ from $\omega(\boldsymbol{n}q_2)$. This allows proceeding to higher q_i, finding $\psi(\boldsymbol{n}q_i/2)$ by linear interpolation if no measurement was taken at $q_i/2$. All calculations were performed ignoring the possible influence of unbalanced terms in Eqs. (2) and (4).

Pore images were obtained by applying an inverse Fourier transform to each radial spoke followed by an inverse Radon transform.

B. Simulations

To investigate the validity of Eqs. (2) and (4) and the influence of the unbalanced terms in the presence of finite gradient timing, Monte Carlo simulations were conducted for triangular pores aligned in the same direction. Rf pulses were realized with rotation matrices. For comparison, the corresponding spin-echo signals were simulated using the Monte Carlo and the multiple correlation function (MCF) approach (Eq. (144) of Ref. [45] and Refs. [36,46–49]) with the analytically known Laplacian eigenfunctions of the triangular domain [36], where accuracy was ensured by gradually increasing the number of eigenfunctions. The following pore distributions with $\int P_{\boldsymbol{x}_{\mathrm{cm}}}(\boldsymbol{x})\, d\boldsymbol{x} = 0$ were chosen:

(1) Rock or tissue sample with a ratio of 80% intraporous space to 20% extraporous space. The specified maximum gradient amplitude was 3.9 T/m, which is available for NMR microimaging systems.

(2) Capillary phantom: A sample was simulated with a fill factor, i.e., ratio of total area inside pore boundaries to sample area, as found in typical capillary phantom experiments such as studied in [27,28,37,50,51]. The fill factor was matched to two phantoms: capillaries with 20 μm inner diameter and 150 μm outer diameter inside a 4 mm NMR tube in [50], and capillaries with 10 μm inner radius and 360 μm outer diameter inside a tube of 8 mm inner diameter in [27,28,37], both yielding a fill factor of 0.003.

(3) Xenon phantom: Pore number and dimensions matched those of the used phantom described in Sec. III C.

For (1)–(3), detailed specifications are tabulated in Table III. The 37 gradient directions were distributed in 5° steps in one half-space of q space. For $\alpha_j = 0$, the relation $S(-\boldsymbol{q}) = S^*(\boldsymbol{q})$ holds true and can be used to calculate the second half-space.

Additionally, two variations of the rock or tissue sample were simulated with narrow homogeneous size distributions: The first was made up of equilateral triangles with mean edge length $L_0 = 10$ μm; the second consisted of cylinders with mean diameter $L_0 = 10$ μm. Both distributions contained 18 500 pores with 100 different pore sizes between $L = 0.75\ L_0$ and $1.25\,L_0$, each size occurring 185 times. Other parameters were chosen identically to (1). In addition, for both distributions, the volume fraction-weighted average pore

TABLE III. Parameters used in simulations of pore distributions.

	Rock or tissue sample	Capillary phantom	Xenon phantom
Triangle edge length L (μm)	10	10	5750
Number of pores	18500	1730	$77 = 7 \times 11$
Sample size (mm × mm)	1 × 1	5 × 5	41 × 79
Pores distributed	Randomly	Randomly	On a square grid
D(μm^2/ms)	1	1	37000
T (ms)	150	150	550
$G_{\max}$ (T/m)	3.9	3.9	32×10^{-3}
δ (ms)	2.88	2.88	2.94
$q_{\max}$ (μm^{-1})	3	3	7×10^{-3}
Pore image	13 × 13 pixels	13 × 13 pixels	19 × 19 pixels
Nominal resolution (μm)	1.05	1.05	449
MCF simulation: Number of q values $N_{q,\mathrm{HS}}$	1000	1000	1000
Monte Carlo simulation:			
Random walkers per pore	2×10^5	5×10^5	1.5×10^6
Steps per random walk trajectory	2.65×10^5	2.65×10^5	1.02×10^6
Number of q values N_q [Δq (μm^{-1})]	20 (0.158)	20 (0.158)	20 (3.68×10^{-4})
α_0 to α_4	0	0	0
Pore images: Number of directions	37 in 5° steps	37 in 5° steps	37 in 5° steps

space function under idealized conditions ($\delta \to 0$, $T \to \infty$) was computed analytically to reconstruct an average pore image, as well as the result for the long-narrow approach [36] using the MCF technique.

Spin-echo signals were rescaled by 1/2 or 1/4 for comparability to account for the signal reduction occurring for stimulated echoes for $\boldsymbol{q} > 0$. Before reconstructing pore images, $S(\boldsymbol{q} = 0)$ for stimulated echoes was also rescaled to avoid a signal jump compared to $S(\boldsymbol{q} > 0)$ in the reconstruction described in Sec. III A.

C. Experimental implementation

For experimental verification of the stimulated echo pore imaging approach, measurements with hyperpolarized xenon-129 gas in phantoms with pores with equilateral triangular cross section were performed. The pores (edge length $L = 5750\,\mu\text{m}$) were arranged on a 7 × 11 grid with gas flowing continuously through the pores (150 ml/min) along the magnetic field direction and orthogonally to the plane, in which the gradients were applied ($G_{\max} = 32$ mT/m; see Table III). Repetition time (TR) was 18 s to ensure sufficient inflow of newly hyperpolarized gas. The high free diffusion coefficient $D_0 = (37\,000 \pm 2000)\,\mu\text{m}^2/\text{ms}$ of the xenon gas mixture [26] allows reaching the long-time limit for pores on the millimeter scale.

Spin-exchange optical pumping (SEOP) was used for hyperpolarization [52–54] and a clinical 1.5 T MR scanner (Magnetom Symphony, A Tim System, Siemens Healthcare, Erlangen, Germany) for measurements. The setup is detailed in Refs. [26,30].

q Space was sampled along radial lines using the stimulated echo sequences depicted in Figs. 1(a) and 1(b). Time intervals t_1 and t_2 between rf pulses and analog-to-digital signal converter (ADC) readout ensure that the center of the stimulated echo and the middle of the readout coincide. As each rf pulse splits magnetization into three parts, i.e., dephasing and rephasing transverse magnetization and the longitudinal magnetization component, the number of coherence pathways increases with each new rf pulse by three per already existing coherence pathway. Counting only those leading to echo formation (spin echo and stimulated echo), five echo pathways remain for a three-pulse sequence. But for a five-pulse sequence, already 58 echo pathways occur [55]. To measure only the desired stimulated echo in the five-pulse double diffusion encoded sequence, rf spoiling and gradient spoiling were used. Following Zur *et al.* [56], rf spoiling was conducted with $\alpha_0 = 117$, $\alpha_1 = 234$, $\alpha_2 = 108$, $\alpha_3 = 99$, $\alpha_4 = 207$, while crusher gradients were applied in the longitudinal storage periods [Figs. 1(a) and 1(b)]. Fluctuations in the polarization level were compensated for by an additional signal prereadout directly after $90^\circ_{\alpha_0}$.

Parameters were chosen as in Table III. Additional specifications were as follows: Duration of the rf pulses was 1.856 ms; to record pore images, 37 radial lines were recorded in one half-space of *q* space with $N_q = 14$ *q* values and $\Delta q = 0.539\,\text{mm}^{-1}$. The second half-space was calculated as described below. For phase cycling, the cycles designed in Tables I and II were used with the rf pulse phases listed for rf spoiling above. For a more detailed view, the vertical gradient direction was additionally measured using a higher number of *q* values ($N_q = 24$) with $q_{\max} = 5\,\text{mm}^{-1}$, $\Delta q = 0.217\,\text{mm}^{-1}$, and $\delta = 2.10$ ms. For the pore images, two repetitions of the rows of Tables I and II were recorded and five repetitions for the vertical direction with $N_q = 24$.

For signal calculation, after normalizing the readout data (average of the echo amplitude) to the prereadout, the two, respectively, five repetitions were averaged and then normalized to $S(\boldsymbol{q}_1 > 0)$. Normalization to $S(\boldsymbol{q}_1)$ was chosen because experimental values for $S(q = 0)$ showed large signal fluctuations potentially due to insufficient dephasing of other coherent pathways. For phase-cycled signals, all averages for all phase cycles were summed up with the respective signs from Tables I and II and then normalized to $S(\boldsymbol{q}_1)$. For reconstruction of $\tilde{\rho}(\boldsymbol{q})$ in case of phase cycling, $S(q = 0)$ was estimated by parabolic extrapolation of the real part of the signal at the first two nonzero q values q_1 and q_2. For comparison, simulated data were also normalized to $\boldsymbol{q}_1$.

For arbitrary α_j, the relation $S(-\boldsymbol{q}) = S^*(\boldsymbol{q})$ was used in the reconstruction although it does not hold true in general. But if only the desired signal term $[\frac{1}{4}e^{i(\alpha_0-\alpha_1-\alpha_2+\alpha_3+\alpha_4)}\tilde{\rho}^*(\boldsymbol{q}/2)^2\tilde{\rho}(\boldsymbol{q})]$ is present, which is the case if phase cycling is used, and if the factor $e^{i(\alpha_0-\alpha_1-\alpha_2+\alpha_3+\alpha_4)}$ is removed by normalization to $S(\boldsymbol{q}_1)$, the relation $S(-\boldsymbol{q}) = S^*(\boldsymbol{q})$ can be used to calculate the second half-space. A pore image from Monte Carlo simulations was computed with the same parameters for comparison.

Simulations, signal processing, and the recursive phase reconstruction from DDE signals were performed in MATLAB (MathWorks, Natick, MA).

IV. RESULTS

Figure 2 shows simulation results. For the rock or tissue sample, $\tilde{P}_{\boldsymbol{x}_{\text{cm}}}(q)$ decays to zero already at small q values [light blue line in Fig. 2(a), left]. Therefore stimulated echo (STE) signals [light blue and light red lines in Fig. 2(a), columns S_3, S_2], calculated by plugging the MCF-simulated form factor into the analytical derivations [Eqs. (2) and (4)], coincide well with the desired MCF-simulated spin-echo (SE) signals (dark lines) considering both real and imaginary part, except for the small q-value region, where the unbalanced terms become evident due to the nonzero $\tilde{P}_{\boldsymbol{x}_{\text{cm}}}(q)$. For higher q values, the undesired terms vanish and the STE signal equals the pure spin-echo term, apart from the reduced magnitude by one half per z-storage interval. Analytical derivations were further checked by simulating STE signals at a lower number of sampling points (dots in the three left columns) with the Monte Carlo method.

The nonvanishing imaginary part of the STE DDE signal allows for calculation of the form factor phase and thus unambiguous image reconstruction. The pore image (right column) for stimulated echoes shows a clearly discernible triangle and hardly deviates from the spin-echo image. Deviations are probably due to Monte Carlo noise.

The distribution resembling capillary phantoms [Fig. 2(b)] has a factor of 10 fewer pores so that the amplitude of $\tilde{P}_{\boldsymbol{x}_{\text{cm}}}(q)$ does not fully decay to zero making the influence of the undesired terms more pronounced. Therefore, the STE

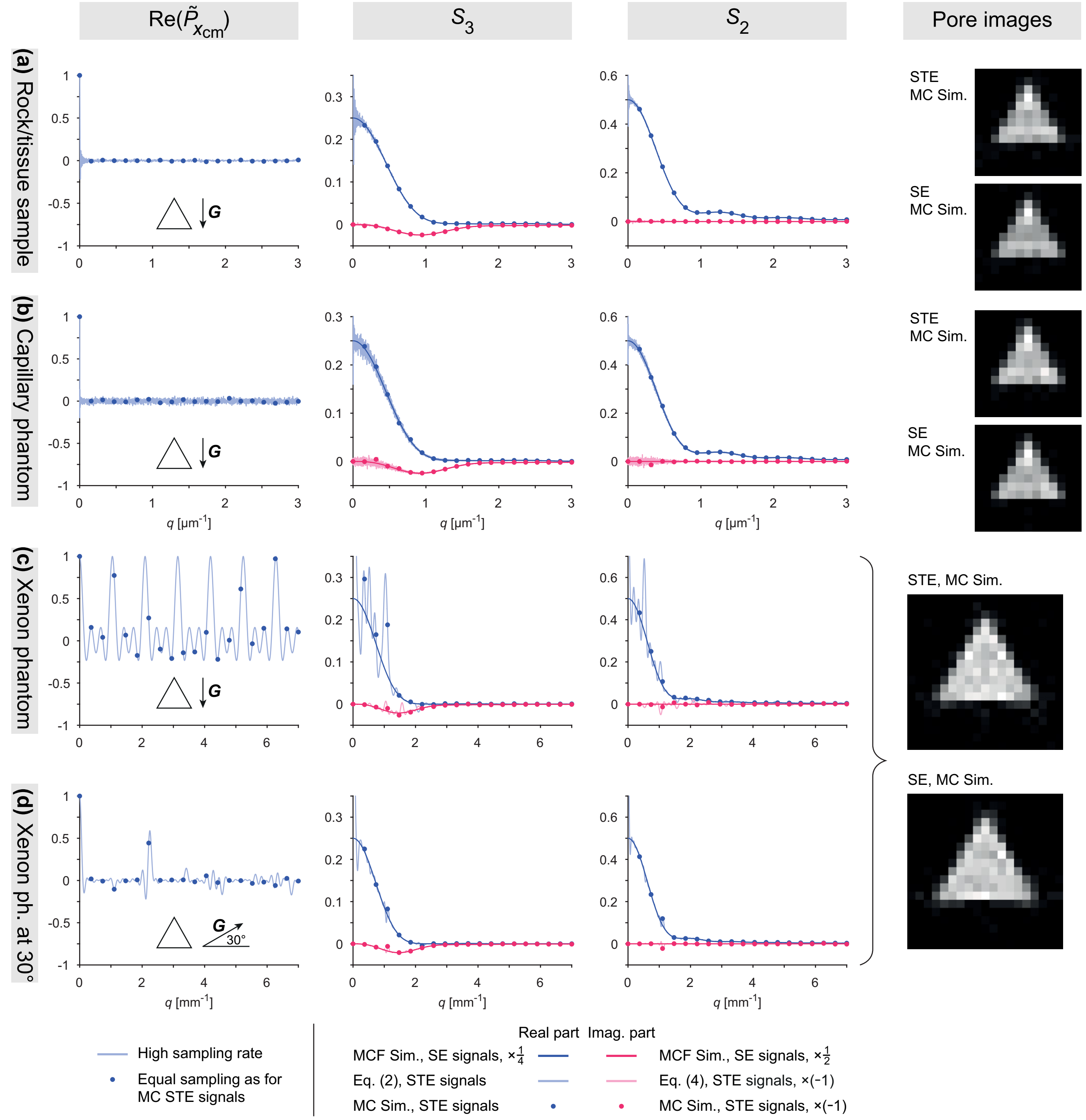

FIG. 2. Simulations for three different pore distributions in (a) to (d): Columns from left to right show the real part of the Fourier transform of the pores' center of mass distribution $\tilde{P}_{x_{\mathrm{cm}}}(q)$, the DDE signals $S_3(q)$, the q-space imaging signals $S_2(q)$, and pore images. For visual comparison, spin-echo magnitudes were reduced by a factor of 4 for DDE signals, by a factor of 2 for q-space imaging, and the negative q-space imaging signal was plotted for stimulated echoes. $\boldsymbol{G}$ indicates the gradient direction relative to the triangular pores. $S_{\mathrm{STE}}(q=0)$ is not displayed due to scaling of axes. Abbreviations used: SE = spin echo, STE = stimulated echo, MCF Sim. = simulations using the multiple correlation function approach, MC Sim. = Monte Carlo simulations.

signals can deviate from the SE signals if a sampling point occasionally hits an outlier of $\tilde{P}_{x_{\mathrm{cm}}}(q)$. Here, the strongest deviation occurs for the imaginary part of the third sampling point of the STE signals from Monte Carlo simulations. The deviation of the STE signals from SE signals is stronger for double diffusion encoding than for q-space imaging (compare light colored lines for S_3 and S_2). Nevertheless, the few and small outliers of the STE signals have little influence on the pore image result.

If the number of pores is decreased further, the contribution of the undesired terms increases. For the xenon phantom and the vertical gradient direction [Fig. 2(c)], the projection onto

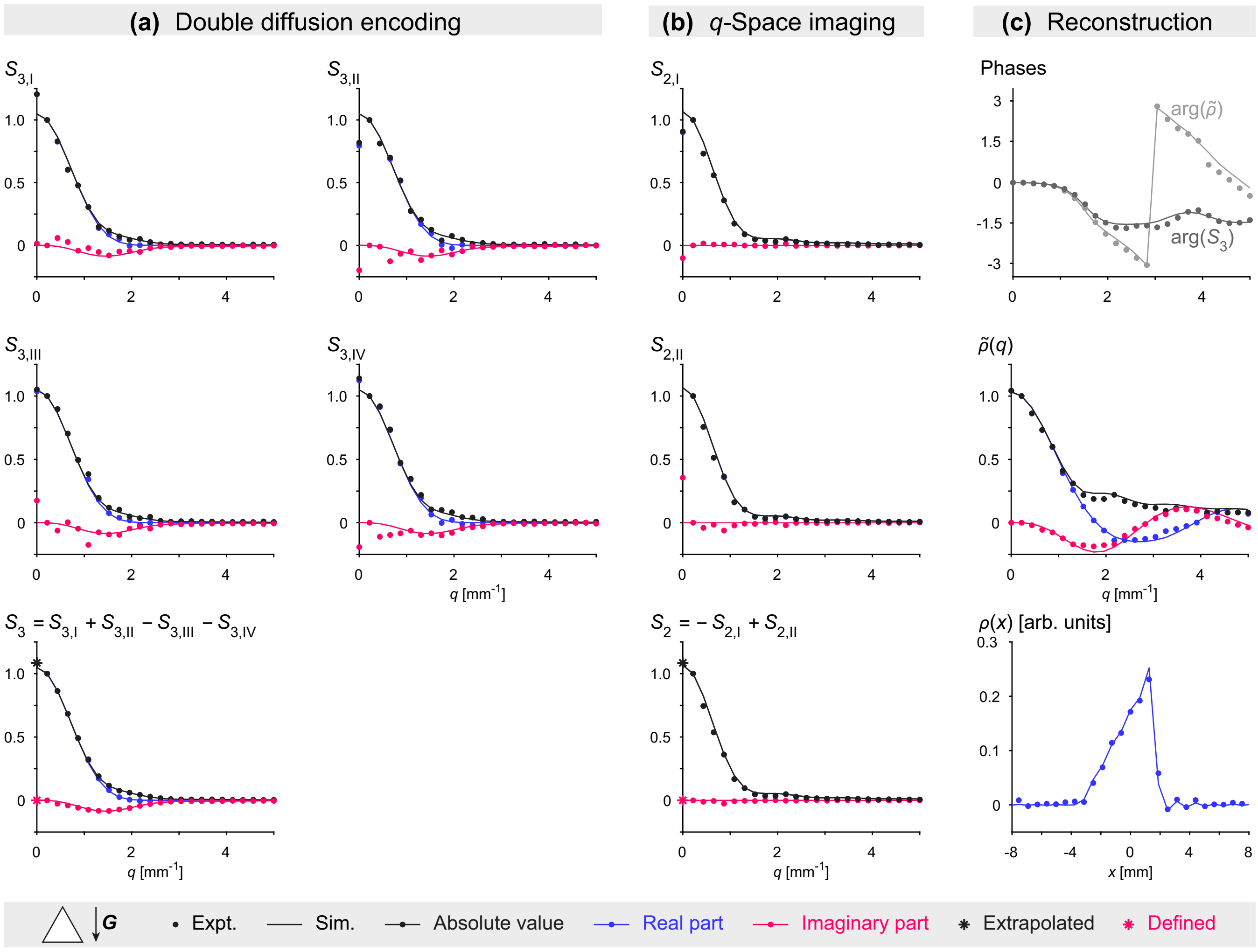

FIG. 3. Experimental results for the phase-cycled stimulated echo DDE signal [(a), dots] and the phase-cycled stimulated echo q-space imaging signal [(b), dots] in comparison to simulated spin-echo signals (lines) for the vertical gradient direction indicated by $\boldsymbol{G}$. For simulations, the MCF method was used with the same sampling points in q space as used in experiments. The individual phase cycle acquisitions and their sums yielding the final signals $S_3(q)$ and $S_2(q)$ are shown. (c) To reconstruct the pore space function $\rho(x)$, the phase of the Fourier transform $\arg[\tilde{\rho}(q)]$ was estimated from $S_3(q)$ while the magnitude $|\tilde{\rho}(q)|$ was calculated from $S_2(q)$.

the gradient direction effectively only shows a distribution of seven pores. For this gradient direction, $\mathrm{Re}[\tilde{P}_{x_{\mathrm{cm}}}(q)]$ shows several local maxima with high amplitude [Fig. 2(c) left column] in contrast to Figs. 2(a) and 2(b), which leads to very strong deviations of the STE signals from the SE signals for $q < 2\,\mathrm{mm}^{-1}$. For $q > 2\,\mathrm{mm}^{-1}$, signal amplitudes are already very low so that high oscillations of $\mathrm{Re}[\tilde{P}_{x_{\mathrm{cm}}}(q)]$ are hardly visible. The gradient vector rotated by 30° [Fig. 2(d)] is oriented relative to the shape of the triangular pores in the same way as the vertical gradient direction and therefore the SE signal decay is identical in Figs. 2(c) and 2(d), but the projection of the pore distribution onto the gradient direction is a result of all 77 pores so that fewer and smaller maxima occur in $\mathrm{Re}[\tilde{P}_{x_{\mathrm{cm}}}(q)]$. Consequently, only one sampling point of the Monte Carlo STE simulation deviates from the SE signal. The fast decay of $\mathrm{Re}[\tilde{P}_{\boldsymbol{x}_{\mathrm{cm}}}(\boldsymbol{q})]$ occurs for most of the sampled radial gradient directions so that these outweigh the vertical and horizontal gradient directions in their contribution to the pore image so that the STE image is nearly identical to the SE version.

The experimental feasibility of the analytically derived STE pore imaging approach was demonstrated with xenon gas in phantom measurements. The results are shown in Fig. 3. For the vertical gradient direction, a nonzero imaginary part arises in the rf-spoiled STE DDE signal $S_{3,\mathrm{I}}(q)$ [red dots in Fig. 3(a) first plot]. The deviations from the simulated SE signal (lines) are clearly visible. However, using a combination of four measurements with complementing rf pulse phases, $S_{3,\mathrm{I}}$ to $S_{3,\mathrm{IV}}$ in Fig. 3(a), the undesired terms can be removed through phase cycling (bottom left plot). The same holds true for q-space imaging [Fig. 3(b)]. Recursively calculating the phase using $\arg(S_3)$ and taking the magnitude from S_2 yields the form factor $\tilde{\rho}(q)$ and one-dimensional pore projection $\rho(x)$ [Fig. 3(c)], which is in good agreement with the SE simulation [solid line in Fig. 3(c)]. Repeating this phase cycling approach for all sampled radial gradient directions in q space yielded the pore image in Fig. 4(a). The triangular pore shape is clearly visible but slightly blurred due to noise. Figure 4(b) shows the corresponding Monte Carlo simulation for comparison.

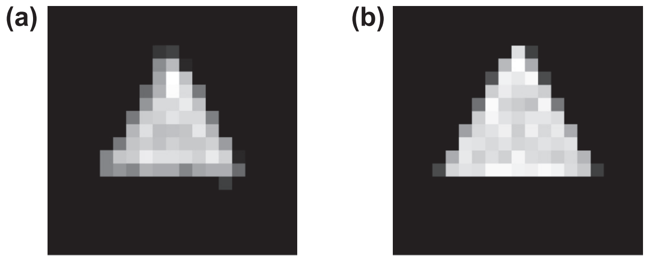

FIG. 4. (a) Measured pore image obtained using stimulated echoes and phase cycling to remove all but the pure spin-echo terms. (b) Corresponding Monte Carlo simulation using stimulated echoes and phase cycling.

Figure 5 shows that the STE approach behaves as the SE version in the presence of pore size distributions: For the considered pore size distributions, a shrinkage is observable compared to the average pore image under idealized conditions ($\delta \rightarrow 0$, $T \rightarrow \infty$), which is mainly due to the edge enhancing effect [43] which becomes apparent in the comparison to the long-narrow approach. Apart from this shrinkage in size, the reconstructed pore images portray good approximations of the average pore image.

V. DISCUSSION

In this study, the signal equation for a double diffusion encoding sequence with stimulated echoes was derived analytically showing that phase information arising for non-point-symmetric pores is preserved in the balanced spin-echo signal term. However, using stimulated echoes always comes at the price of introducing additional undesired unbalanced terms that can potentially distort the total signal. If the undesired terms are either negligible or are removed (see discussion below), DDE-based diffusion pore imaging with stimulated echoes is enabled. Moreover, applicability of stimulated echoes to complex signals is not only relevant to pore imaging but, in principle, of interest to all fields where signal phases arise. The analytical derivation was validated with Monte Carlo simulations for a non-point-symmetric triangle domain for which nonvanishing imaginary parts arise in the DDE signals. In addition, an experimental demonstration of the STE pore imaging approach was conducted with hyperpolarized xenon.

In principle, the unbalanced terms modulated with the Fourier transform of the pores' center of mass distribution $\tilde{P}_{\boldsymbol{x}_{\mathrm{cm}}}(\boldsymbol{q})$ can disturb complex phase information obtained from the DDE signal and induce a dependence of the stimulated echo signals on the absolute positions of the pores in the gradient system. For all applications to natural samples with randomly distributed pores and imaging volume elements large compared to the pore sizes, the phase information needed to perform DDE-based pore imaging is practically undisturbed by the unbalanced terms, so that these can be neglected in the same way as for conventional diffusion-based techniques considering the magnitude only. For medium sized samples like capillary phantoms, small deviations from the spin-echo curve might be observed. However, for ordered samples with a very low number of pores local maxima with high amplitudes can occur in $\tilde{P}_{\boldsymbol{x}_{\mathrm{cm}}}(\boldsymbol{q} > 0)$. In the latter case, deviations are strongest in only a few of the radial gradient directions for which the projection of the distribution onto the gradient direction forms a pattern concealing a fraction of the pores. However, as multiple radial directions are recorded to acquire pore images, most of the directions do not point along the main symmetry axes, so that a larger number of different $\boldsymbol{x}_{\mathrm{cm}}$ positions are projected on those directions yielding fast decaying unbalanced terms, so that these undisturbed directions will dominate in the reconstruction of pore images. Moreover, in experiments, $\tilde{P}_{\boldsymbol{x}_{\mathrm{cm}}}(\boldsymbol{q})$-based deviations might be additionally suppressed due to inhomogeneity of the gradient field causing averaging over a small span of q values and thus effectively smoothing the stimulated echo signals.

If deviations caused by nonvanishing unbalanced signal terms are observed, a suitable selective phase cycle can be applied in the same way as for signal magnitude-based approaches as proposed by Khrapitchev and Callaghan. One downside of the phase cycling approach is that the measurement time increases by a factor of 4 for double diffusion encoding, and doubles for q-space imaging. However, by making use of this approach, it can be concluded that DDE-based pore imaging with stimulated echoes can in principle be applied to every type of sample, as either unbalanced signal terms are too small to contribute to the total signal or otherwise they cause deviations from the desired spin-echo term but an appropriate phase cycling scheme can be used to eliminate them.

The deviation of the STE echo signals from SE signals are in principle stronger for double diffusion encoding than for q-space imaging because three terms modulated with $\tilde{P}_{\boldsymbol{x}_{\mathrm{cm}}}(\boldsymbol{q})$ or $\tilde{P}_{\boldsymbol{x}_{\mathrm{cm}}}(2\boldsymbol{q})$ arise for the DDE signal in addition to the spin-echo term, whereas only one term modulated with $\tilde{P}^{*}_{\boldsymbol{x}_{\mathrm{cm}}}(2\boldsymbol{q})$ contributes to the q-space signal.

A disadvantage of the stimulated echo method, specifically, is the relative signal intensity of $1/2$ for q-space imaging and $1/4$ for double diffusion encoding when compared to the respective spin-echo signals [9,15]. In addition, various challenges arise for pore imaging in general when moving from well-defined pore phantoms to tissue samples such as physiological noise, cell membrane permeability, signal arising from extracellular water compartments, surface relaxation

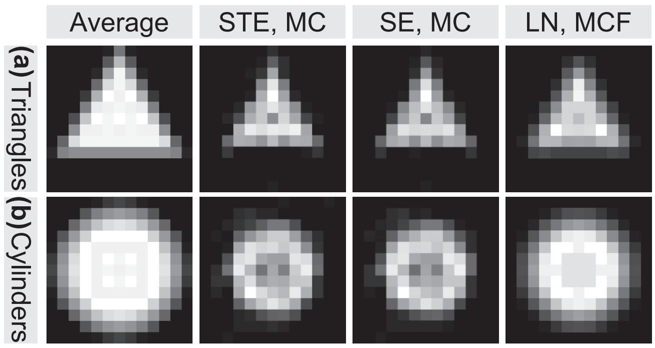

FIG. 5. Simulations of size distributions of (a) triangles and (b) cylinders. Columns: (1) Volume fraction-weighted average pore image for $\delta \rightarrow 0$, $T \rightarrow \infty$; (2) Monte Carlo simulation using stimulated echoes; (3) Monte Carlo simulation using spin echoes; (4) MCF simulation using the long-narrow approach.

[36,39], or open connected geometries [57]. But a major challenge of diffusion pore imaging lies in resolving pore size and shape distributions. A direct inversion from an average pore space function to the underlying distribution of individual pore space functions poses, so far, an open problem. Fortunately, for the proposed STE technique, no additional complications arise concerning size and shape distributions compared to spin echoes, which were discussed in detail in [43]: For the short gradient method combing DDE and q-space measurements applied in this work to narrow size distributions, the signal is dominated by the pores with small volume fractions while larger pores are underestimated so that the reconstructed image exhibits a pronounced shrinkage compared to the volume fraction-weighted average image. Further, pore shape-specific artifacts such as underestimated signal intensities in specific areas of the image can occur. An image closer to the true average pore image can be obtained with the long-narrow approach with finite timing parameters. However, the requirement of the long-narrow approach that the diffusion distance during the long pulse needs to be sufficiently large to probe the whole pore imposes limitations on pore sizes that can potentially be measured.

High gradient amplitudes are mandatory to perform pore imaging at the micrometer scale [36] but are generally unavailable in clinical MRI machines. However, stimulated echo sequences can partially solve the unavailability of gradient power for larger pore sizes: The demand on gradient strength reduces quadratically with pore diameter and, with stimulated echoes, the diffusion time can be increased without pronounced signal decay through T_2 relaxation effects by instead exploiting the typically long T_1 relaxation time so that the diffusion long-time limit can be reached in the larger sized pores. This is feasible because DDE-based pore imaging uses only short gradient pulses between which magnetization can be stored longitudinally opposed to the long-narrow pore imaging approach, which requires the application of very long gradient pulses filling most of the diffusion time.

For example, demands on diffusion time and gradient strength might be met on whole-body scanners with amplitudes of 45 mT/m for imaging of muscle cells, which have much larger diameters than most cells (~50 μm), using phosphocreatine as the tracer. In muscle tissue, T_2 is quite short unlike T_1, so that stimulated echoes may be used as a tool to reach the diffusion long-time limit in muscle cells [58–60]. Another feasible application could be diffusion of N-acetylaspartic acid (NAA) in the soma of a neuron with a soma diameter of 10 μm for 1.5 T/m gradients available for small animal scanners [61–64]. However, the above listed general pore imaging challenges remain before an application *in vivo* may become feasible with this work being just one step in that direction.

The stimulated echo z-storage periods add another beneficial side effect: As a result of the shortened residence time of the spins in the transverse plane, spins located in areas affected by field inhomogeneities will collect smaller phases as if the phases would accumulate over the total diffusion time which could cause image warping or blurring.

In conclusion, using stimulated echoes in diffusion pore imaging is feasible, thus opening the possibility to use longer diffusion times by exploiting T_1 relaxation.

ACKNOWLEDGMENT

Financial support by the DFG (Grants No. KU 3362/1-1 and No. LA 2804/6-1) is gratefully acknowledged.

APPENDIX: STIMULATED ECHO SIGNALS FOR DOUBLE DIFFUSION ENCODING AND *q*-SPACE IMAGING

Here, we provide a detailed derivation of Eqs. (2) and (4).

A pulse sequence, composed of radiofrequency pulses and gradient pulses, imprints specific phase factors on diffusing spin packets. These can be derived by sequentially applying building blocks for (a) short gradient pulses, and (b) two rf pulses generating stimulated echoes. Both are applied to the preexisting transverse magnetization $e^{i\varphi}$ of the considered spin packet:

(a) A gradient pulse $\boldsymbol{G}_i$ of duration δ induces a phase factor $e^{i\varphi_i}$ to spins with

$$\varphi_i = -\gamma \int_0^\delta \boldsymbol{G}_i\, \boldsymbol{x}(t) dt = -\gamma \delta \boldsymbol{G}_i \boldsymbol{x}_{i,\text{path}}, \tag{A1}$$

where γ is the gyromagnetic ratio and $\boldsymbol{x}_{i,\text{path}}$ the center of mass of the path that is traveled by the random walker during the application of the gradient pulse [65]. In the limit of short gradient pulses ($\delta \rightarrow 0$), $\boldsymbol{x}_{i,\text{path}}$ is replaced with the position $\boldsymbol{x}_i$ of the spins during gradient application. If the pore's center of mass is translated from the origin to $\boldsymbol{x}_{\text{cm}}$, additional global phase shifts ϑ_i occur. The effect of a short gradient pulse ($\delta \rightarrow 0$) is given by

$$e^{i\varphi} \rightarrow e^{i(\varphi+\varphi_i+\vartheta_i)}. \tag{A2}$$

(b) For the time being, only rf pulses with fixed flip angles of 90° but variable pulse phases α_j are considered. α_j defines the rotation axis of the 90° rf pulses [see Fig. 1(c)], in which the coordinate system is defined. Assume that two perfect rf pulses separated by the storage time τ, i.e., $(90^\circ_{\alpha_1} - \tau - 90^\circ_{\alpha_2})$ as, e.g., used in Figs. 1(a) and 1(b), are applied to a transverse magnetization $e^{i\varphi}$. The first pulse $90^\circ_{\alpha_1}$ rotates the magnetization by 90° around the axis given by α_1. It is assumed that the z-storage period τ is long enough to sufficiently dephase the transverse magnetization. The stored magnetization in the z direction has the same magnitude as the component of the magnetization vector that is orthogonal to the effective magnetic field during application of the $90^\circ_{\alpha_1}$ pulse. The z magnetization can be calculated by describing the $90^\circ_{\alpha_1}$ pulse as a rotation around the z axis by $-\alpha_1$ followed by a 90° rotation around the x axis and omission of transverse components. Thus, the magnitude of the stored z magnetization is given by $\text{Re}(e^{i(\varphi-\alpha_1)})$. The z magnetization is returned to the transverse plane by $90^\circ_{\alpha_2}$, which effectively flips the magnetization to lie along the negative real axis followed by a rotation by α_2, resulting in $\text{Re}(-e^{i(\varphi-\alpha_1)})e^{i\alpha_2} = -\cos(\varphi-\alpha_1)e^{i\alpha_2}$. Rewriting in terms of the exponential function shows that the number of terms doubles and a factor $\frac{1}{2}$ is introduced for each $(90^\circ_{\alpha_1} - \tau - 90^\circ_{\alpha_2})$ sequence:

$$e^{i\varphi} \rightarrow -\tfrac{1}{2}\left(e^{i(\varphi-\alpha_1+\alpha_2)} + e^{-i(\varphi-\alpha_1-\alpha_2)}\right). \tag{A3}$$

For examples, see [14,44].

A DDE sequence with stimulated echoes [Fig. 1(a)] where all rf pulses are applied along the x axis, i.e., $\alpha_0 = \alpha_1 =$

$\alpha_2 = \alpha_3 = \alpha_4 = 0$, and with gradient vectors $\boldsymbol{G}_1/2$ applied at $t = 0$, $\boldsymbol{G}_2$ at $t = (T - \delta)/2$, and $\boldsymbol{G}_3/2$ applied at $t = T - \delta$ with $\boldsymbol{G}_1 = \boldsymbol{G}_2 = \boldsymbol{G}_3$, is considered first: The initial excitation pulse generates real magnetization pointing along the y axis. Applying the first gradient to a pore translated from the origin [Eq. (A2)] leads to the phase factor $e^{i(\frac{\varphi_1}{2}+\frac{\vartheta}{2})}$ with $\vartheta = 2\vartheta_1 = 2\vartheta_3 = \vartheta_2 = -\gamma\delta\boldsymbol{G}_2\boldsymbol{x}_{\text{cm}}$. The next block $(90^\circ_0 - \tau - 90^\circ_0)$ results, according to Eq. (A3), in $-\frac{1}{2}(e^{i(\frac{\varphi_1}{2}+\frac{\vartheta}{2})} + e^{-i(\frac{\varphi_1}{2}+\frac{\vartheta}{2})})$. Applying Eqs. (A2) and (A3) for G_2, $(90^\circ_0 - \tau - 90^\circ_0)$, and $G_3/2$, leads to the final phase factor composed of four terms and a factor of $\frac{1}{4}$:

$$\begin{aligned}\tfrac{1}{4}\Big\{&e^{i(\frac{\varphi_1}{2}-\varphi_2+\frac{\varphi_3}{2})} + e^{i(\frac{\varphi_1}{2}+\varphi_2+\frac{\varphi_3}{2}+2\vartheta)}\\ &+e^{i(-\frac{\varphi_1}{2}-\varphi_2+\frac{\varphi_3}{2}-\vartheta)} + e^{i(-\frac{\varphi_1}{2}+\varphi_2+\frac{\varphi_3}{2}+\vartheta)}\Big\}.\end{aligned} \tag{A4}$$

Equation (A4) is the same as Eq. (1). A similar equation was derived in [14]. However, in the following, the special case of a set of closed pores is considered with focus on the final signal phase which was not investigated so far. The ensemble average of the first term yields $S_{3,\text{STE},1} = \langle \frac{1}{4} e^{i(\frac{\varphi_1}{2}-\varphi_2+\frac{\varphi_3}{2})}\rangle = \frac{1}{4}S_{3,\text{SE}}$ with $S_{3,\text{SE}}$ being the desired compensated signal that arises for a spin-echo sequence with a 180° pulse inserted after the second gradient pulse and opposite gradient vector of the first pulse given by Eq. (3). Using Eq. (A1) and introducing the q vector $\boldsymbol{q} = -\gamma\boldsymbol{G}_2\delta$, the first term is rewritten to $S_{3,\text{STE},1}(\boldsymbol{q}) = \langle \frac{1}{4} e^{i\boldsymbol{q}(\frac{\boldsymbol{x}_{1,\text{path}}}{2} - \boldsymbol{x}_{2,\text{path}} + \frac{\boldsymbol{x}_{3,\text{path}}}{2})}\rangle$. Assuming $\delta \to 0$, the centers of mass of the respective particle trajectories during the gradient pulses are replaced by $\boldsymbol{x}_1 = \boldsymbol{x}(0)$, $\boldsymbol{x}_2 = \boldsymbol{x}(T/2)$, and $\boldsymbol{x}_3 = \boldsymbol{x}(T)$, yielding $S_{3,\text{STE},1}(\boldsymbol{q}) = \langle \frac{1}{4} e^{i\boldsymbol{q}(\frac{\boldsymbol{x}_1}{2} - \boldsymbol{x}_2 + \frac{\boldsymbol{x}_3}{2})}\rangle$. A large number N of closed pores is considered, where the distribution of the pores' center of mass is described by $P_{\boldsymbol{x}_{\text{cm}}}(\boldsymbol{x}_{\text{cm}})$. The ensemble average is then the average over all possible random walk trajectories in all pores resulting in

$$\begin{aligned}S_{3,\text{STE},1}(\boldsymbol{q}) = \tfrac{1}{4}&\int_{\mathbb{R}^3} d\boldsymbol{x}_{\text{cm}} \int_{\text{Pore}} d\boldsymbol{x}_1 \int_{\text{Pore}} d\boldsymbol{x}_2 \int_{\text{Pore}} d\boldsymbol{x}_3 P_{\boldsymbol{x}_{\text{cm}}}(\boldsymbol{x}_{\text{cm}})\\ &\times \rho(\boldsymbol{x}_1)\rho(\boldsymbol{x}_2)\rho(\boldsymbol{x}_3)e^{i\boldsymbol{q}(\frac{\boldsymbol{x}_1}{2}-\boldsymbol{x}_2+\frac{\boldsymbol{x}_3}{2})}.\end{aligned} \tag{A5}$$

In the diffusion long-time limit $(T \to \infty)$, $\boldsymbol{x}_1$, $\boldsymbol{x}_2$, and $\boldsymbol{x}_3$ are uncorrelated, so that averaging independently over each $\boldsymbol{x}_i$ becomes possible:

$$\begin{aligned}S_{3,\text{STE},1}(\boldsymbol{q}) &= \frac{1}{4}\int_{\mathbb{R}^3} d\boldsymbol{x}_{\text{cm}} P_{\boldsymbol{x}_{\text{cm}}}(\boldsymbol{x}_{\text{cm}}) \int_{\text{Pore}} d\boldsymbol{x}_1 \rho(\boldsymbol{x}_1) e^{i\boldsymbol{q}\frac{\boldsymbol{x}_1}{2}}\\ &\quad\times \int_{\text{Pore}} d\boldsymbol{x}_2 \rho(\boldsymbol{x}_2) e^{-i\boldsymbol{q}\boldsymbol{x}_2} \int_{\text{Pore}} d\boldsymbol{x}_3 \rho(\boldsymbol{x}_3) e^{i\boldsymbol{q}\frac{\boldsymbol{x}_3}{2}}\\ &= \frac{1}{4}\tilde{\rho}^*(\boldsymbol{q}/2)\tilde{\rho}(\boldsymbol{q})\tilde{\rho}^*(\boldsymbol{q}/2) = \frac{1}{4}\tilde{\rho}^*(\boldsymbol{q}/2)^2\tilde{\rho}(\boldsymbol{q}),\end{aligned} \tag{A6}$$

where the asterisk denotes the complex conjugate. Since $S_{3,\text{STE},1}(\boldsymbol{q})$ describes the balanced term (which is equal to the signal arising for a spin-echo sequence with balanced gradients), phases from translations cancel out and the distribution $P_{\boldsymbol{x}_{\text{cm}}}(\boldsymbol{x}_{\text{cm}})$ disappears in Eq. (A6) due to $\int_{\mathbb{R}^3} d\boldsymbol{x}_{\text{cm}} P_{\boldsymbol{x}_{\text{cm}}}(\boldsymbol{x}_{\text{cm}}) = 1$. Averaging over $\boldsymbol{x}_{\text{cm}}$ introduces the Fourier transform of the pores' center of mass distribution $\tilde{P}_{\boldsymbol{x}_{\text{cm}}}(\boldsymbol{q})$ as prefactors in the three undesired terms; i.e., the stimulated echo signal is depending on the absolute positions of the pores because the ϑ_i arising from unbalanced gradient contributions in Eq. (A2) do not cancel out. Here, the ensemble average of the second term of Eq. (A4) is used as an example, derived in analogy to Eq. (A6) using the definition of ϑ:

$$\begin{aligned}S_{3,\text{STE},2}(\boldsymbol{q}) &= \frac{1}{4}\int_{\mathbb{R}^3} d\boldsymbol{x}_{\text{cm}} P_{\boldsymbol{x}_{\text{cm}}}(\boldsymbol{x}_{\text{cm}}) e^{i\boldsymbol{q}2\boldsymbol{x}_{\text{cm}}} \tilde{\rho}^*(\boldsymbol{q}/2)^2\tilde{\rho}^*(\boldsymbol{q})\\ &= \frac{1}{4}\tilde{P}^*_{\boldsymbol{x}_{\text{cm}}}(2\boldsymbol{q})\tilde{\rho}^*(\boldsymbol{q}/2)^2\tilde{\rho}^*(\boldsymbol{q}).\end{aligned} \tag{A7}$$

The total DDE signal with stimulated echoes is

$$\begin{aligned}S_{3,\text{STE}}(\boldsymbol{q}) = \tfrac{1}{4}\{&\tilde{\rho}^*(\boldsymbol{q}/2)^2\tilde{\rho}(\boldsymbol{q}) + \tilde{P}^*_{\boldsymbol{x}_{\text{cm}}}(2\boldsymbol{q})\tilde{\rho}^*(\boldsymbol{q}/2)^2\tilde{\rho}^*(\boldsymbol{q})\\ &+ \tilde{P}_{\boldsymbol{x}_{\text{cm}}}(\boldsymbol{q})|\tilde{\rho}(\boldsymbol{q}/2)|^2\tilde{\rho}(\boldsymbol{q})\\ &+ \tilde{P}^*_{\boldsymbol{x}_{\text{cm}}}(\boldsymbol{q})|\tilde{\rho}(\boldsymbol{q}/2)|^2\tilde{\rho}^*(\boldsymbol{q})\}.\end{aligned} \tag{A8}$$

For the q-space sequence with stimulated echoes [Fig. 1(b), $\alpha_0 = \alpha_1 = \alpha_2 = 0$, $\boldsymbol{G}_1 = \boldsymbol{G}_2$ at $t = 0$ and $t = T - \delta$], the signal is derived in the same manner. Two phase factor terms arise,

$$-\tfrac{1}{2}(e^{i(-\varphi_1+\varphi_2)} + e^{i(\varphi_1+\varphi_2+2\vartheta)}), \tag{A9}$$

which result in

$$S_{2,\text{STE}}(\boldsymbol{q}) = -\tfrac{1}{2}\{|\tilde{\rho}(\boldsymbol{q})|^2 + \tilde{P}^*_{\boldsymbol{x}_{\text{cm}}}(2\boldsymbol{q})\tilde{\rho}^*(\boldsymbol{q})^2\}. \tag{A10}$$

As three 90° pulses with the x axis as the rotation axis were applied, the magnetization vector points along the negative y axis resulting in the minus sign in Eq. (A10).

Still considering the special case with $\alpha_j = 0$, the polarity of the diffusion-encoding gradients can in principle be chosen arbitrarily for stimulated echoes, i.e., all parallel as above, or one or multiple of the gradient directions can be chosen to point along the antiparallel direction. In the case where the last gradient $\boldsymbol{G}$ is replaced by $-\boldsymbol{G}$ the complex conjugate signals will be measured, $S^*_{3,\text{STE}}(\boldsymbol{q})$, respectively $S^*_{2,\text{STE}}(\boldsymbol{q})$.

For the general case with arbitrary rf pulse phases α_j in Eq. (A3), Eqs. (A8) and (A10) extend to Eqs. (2) and (4). Different α_j yield different superpositions of the four terms of the DDE signal (see Table I), respectively, of the two terms of the q-space signal (Table II).

[1] Y. Guo, Y. Q. Cai, Z. L. Cai, Y. G. Gao, N. Y. An, L. Ma, S. Mahankali, and J. H. Gao, J. Magn. Reson. Imaging **16**, 172 (2002).

[2] E. Goebell, S. Paustenbach, O. Vaeterlein, X.-Q. Ding, O. Heese, J. Fiehler, T. Kucinski, C. Hagel, M. Westphal, and H. Zeumer, Radiology **239**, 217 (2006).

[3] A. Lemke, F. B. Laun, M. Klauss, T. J. Re, D. Simon, S. Delorme, L. R. Schad, and B. Stieltjes, Invest. Radiol. **44**, 769 (2009).

[4] A. R. Padhani, D. M. Koh, and D. J. Collins, Radiology **261**, 700 (2011).

[5] J. Hillengass, T. Bäuerle, R. Bartl, M. Andrulis, F. McClanahan, F. B. Laun, C. M. Zechmann, R. Shah, B. Wagner-Gund, D. Simon *et al.*, Br. J. Haematol. **153**, 721 (2011).

[6] A. B. Rosenkrantz, E. E. Sigmund, G. Johnson, J. S. Babb, T. C. Mussi, J. Melamed, S. S. Taneja, V. S. Lee, and J. H. Jensen, Radiology **264**, 126 (2012).

[7] M. C. Roethke, T. A. Kuder, T. H. Kuru, M. Fenchel, B. A. Hadaschik, F. B. Laun, H. P. Schlemmer, and B. Stieltjes, Invest. Radiol. **50**, 483 (2015).

[8] S. Bickelhaupt, F. B. Laun, J. Tesdorff, W. Lederer, H. Daniel, A. Stieber, S. Delorme, and H. P. Schlemmer, Radiology **278**, 689 (2016).

[9] E. L. Hahn, Phys. Rev. **80**, 580 (1950).

[10] K. D. Merboldt, W. Hanicke, and J. Frahm, J. Magn. Reson. (1969) **64**, 479 (1985).

[11] J. E. Tanner, J. Chem. Phys. **52**, 2523 (1970).

[12] K. D. Merboldt, W. Hanicke, and J. Frahm, Magn. Reson. Med. **19**, 233 (1991).

[13] K. D. Merboldt, W. Hanicke, H. Bruhn, M. L. Gyngell, and J. Frahm, Magn. Reson. Med. **23**, 179 (1992).

[14] A. A. Khrapitchev and P. T. Callaghan, J. Magn. Reson. **152**, 259 (2001).

[15] J. Hennig, K. A. Il'yasov, and M. Weigel, Magn. Reson. Med. **68**, 1157 (2012).

[16] A. M. Marschar, T. A. Kuder, B. Stieltjes, A. M. Nagel, P. Bachert, and F. B. Laun, J. Magn. Reson. Imaging **41**, 1581 (2015).

[17] A. Merrem, S. Hofer, D. Voit, K.-D. Merboldt, J. Klosowski, M. Untenberger, J. Fleischhammer, and J. Frahm, Invest. Radiol. **52**, 428 (2017).

[18] Y. Gao, F. Han, Z. Zhou, X. Zhong, X. Bi, J. Neylon, A. Santhanam, Y. Yang, and P. Hu, Magn. Reson. Med. **81**, 2374 (2019).

[19] A. Merrem, S. Hofer, A. S. A. Hosseini, D. Voit, K.-D. Merboldt, Z. Tan, and J. Frahm, NMR Biomed. **32**, e4074 (2019).

[20] D. K. Jones, *Diffusion MRI: Theory, Methods, and Applications* (Oxford University Press, New York, 2011).

[21] E. Fieremans, L. M. Burcaw, H. H. Lee, G. Lemberskiy, J. Veraart, and D. S. Novikov, NeuroImage **129**, 414 (2016).

[22] E. Fieremans, G. Lemberskiy, J. Veraart, E. E. Sigmund, S. Gyftopoulos, and D. S. Novikov, NMR Biomed **30**, e3612 (2016).

[23] G. Lemberskiy, A. Rosenkrantz, J. Veraart, S. S. Taneja, D. Novikov, and E. Fieremans, Invest. Radiol. **52**, 405 (2017).

[24] E. Özarslan and P. J. Basser, J. Magn. Reson. **188**, 285 (2007).

[25] F. B. Laun, T. A. Kuder, W. Semmler, and B. Stieltjes, Phys. Rev. Lett. **107**, 048102 (2011).

[26] T. A. Kuder, P. Bachert, J. Windschuh, and F. B. Laun, Phys. Rev. Lett. **111**, 028101 (2013).

[27] S. Hertel, M. Hunter, and P. Galvosas, Phys. Rev. E **87**, 030802(R) (2013).

[28] S. A. Hertel, M. Hunter, and P. Galvosas, Microporous Mesoporous Mater. **205**, 44 (2015).

[29] S. A. Hertel and P. Galvosas, J. Magn. Reson. **275**, 90 (2017).

[30] K. Demberg, F. B. Laun, J. Windschuh, R. Umathum, P. Bachert, and T. A. Kuder, Phys. Rev. E **95**, 022404 (2017).

[31] M. Bertleff, S. Domsch, F. B. Laun, T. A. Kuder, and L. R. Schad, J. Magn. Reson. **278**, 39 (2017).

[32] K. Demberg, F. B. Laun, M. Bertleff, P. Bachert, and T. A. Kuder, Phys. Rev. E **97**, 052412 (2018).

[33] A. Jerschow and N. Müller, J. Magn. Reson. **125**, 372 (1997).

[34] N. Shemesh, E. Özarslan, T. Adiri, P. J. Basser, and Y. Cohen, J. Chem. Phys. **133**, 044705 (2010).

[35] N. Shemesh and Y. Cohen, J. Magn. Reson. **212**, 362 (2011).

[36] F. B. Laun, T. A. Kuder, A. Wetscherek, B. Stieltjes, and W. Semmler, Phys. Rev. E **86**, 021906 (2012).

[37] S. A. Hertel, X. Wang, P. Hosking, M. C. Simpson, M. Hunter, and P. Galvosas, Phys. Rev. E **92**, 012808 (2015).

[38] N. Shemesh, C. F. Westin, and Y. Cohen, Phys. Rev. Lett. **108**, 058103 (2012).

[39] T. A. Kuder and F. B. Laun, Magn. Reson. Med. **70**, 836 (2013).

[40] P. T. Callaghan, A. Coy, D. Macgowan, K. J. Packer, and F. O. Zelaya, Nature **351**, 467 (1991).

[41] N. Shemesh, S. N. Jespersen, D. C. Alexander, Y. Cohen, I. Drobnjak, T. B. Dyrby, J. Finsterbusch, M. A. Koch, T. Kuder, F. Laun *et al.*, Magn. Reson. Med. **75**, 82 (2016).

[42] F. B. Laun and T. A. Kuder, Magn. Reson. Imaging **31**, 1236 (2013).

[43] T. A. Kuder and F. B. Laun, Phys. Rev. E **92**, 022706 (2015).

[44] P. T. Callaghan, *Translational Dynamics and Magnetic Resonance: Principles of Pulsed Gradient Spin Echo NMR* (Oxford University Press, Oxford, UK, 2011).

[45] D. S. Grebenkov, Rev. Mod. Phys. **79**, 1077 (2007).

[46] A. Caprihan, L. Z. Wang, and E. Fukushima, J. Magn. Reson., Ser. A **118**, 94 (1996).

[47] P. T. Callaghan, J. Magn. Reson. **129**, 74 (1997).

[48] A. V. Barzykin, J. Magn. Reson. **139**, 342 (1999).

[49] D. S. Grebenkov, Concepts Magn. Reson., Part A **32A**, 277 (2008).

[50] L. Avram, Y. Assaf, and Y. Cohen, J. Magn. Reson. **169**, 30 (2004).

[51] A. Bar-Shir, L. Avram, E. Özarslan, P. J. Basser, and Y. Cohen, J. Magn. Reson. **194**, 230 (2008).

[52] T. G. Walker and W. Happer, Rev. Mod. Phys. **69**, 629 (1997).

[53] N. J. Shah, T. Unlu, H. P. Wegener, H. Halling, K. Zilles, and S. Appelt, NMR Biomed **13**, 214 (2000).

[54] A. M. Oros and N. J. Shah, Phys. Med. Biol. **49**, R105 (2004).

[55] R. J. Nelson, Y. Maguire, D. F. Caputo, G. Leu, Y. Kang, M. Pravia, D. Tuch, S. Weinstein, and D. G. Cory, Concepts Magn. Reson. **10**, 331 (1998).

[56] Y. Zur, M. L. Wood, and L. J. Neuringer, Magn. Reson. Med. **21**, 251 (1991).

[57] F. B. Laun, L. Müller, and T. A. Kuder, Phys. Rev. E **93**, 032401 (2016).

[58] R. A. de Graaf, A. van Kranenburg, and K. Nicolay, Biophys. J. **78**, 1657 (2000).

[59] R. E. Gabr, A. M. El-Sharkawy, M. Schar, R. G. Weiss, and P. A. Bottomley, Am. J. Physiol.: Cell Physiol. **301**, C234 (2011).

[60] W. Bogner, M. Chmelik, A. I. Schmid, E. Moser, S. Trattnig, and S. Gruber, Magn. Reson. Med. **62**, 574 (2009).

[61] C. D. Kroenke, J. J. Ackerman, and D. A. Yablonskiy, Magn. Reson. Med. **52**, 1052 (2004).

[62] J. Upadhyay, K. Hallock, K. Erb, D. S. Kim, and I. Ronen, Magn. Reson. Med. **58**, 1045 (2007).

[63] E. T. Wood, E. Ercan, P. Sati, I. C. M. Cortese, I. Ronen, and D. S. Reich, Neuroimage: Clin. **15**, 780 (2017).

[64] J. Valette, C. Ligneul, C. Marchadour, C. Najac, and M. Palombo, Front. Neurosci. **12** (2018).

[65] P. P. Mitra and B. I. Halperin, J. Magn. Reson., Ser. A **113**, 94 (1995).